

Regular Article - Soft Matter

Stretching Hookean ribbons part I: relative edge extension underlies transverse compression and buckling instability

Meng Xin and Benny Davidovitch^a

Physics Department, University of Massachusetts, Amherst, MA 01003, USA

Received 24 December 2020 / Accepted 17 June 2021 \odot The Author(s), under exclusive licence to EDP Sciences, SIF and Springer-Verlag GmbH Germany, part of Springer Nature 2021

Abstract The wrinkle pattern exhibited upon stretching a rectangular sheet has attracted considerable interest in the "extreme mechanics" community. Nevertheless, key aspects of this notable phenomenon remain elusive. Specifically—what is the origin of the compressive stress underlying the instability of the planar state? what is the nature of the ensuing bifurcation? how does the shape evolve from a critical, near-threshold regime to a fully developed pattern of parallel wrinkles that permeate most of the sheet? In this paper we address some of these questions through numerical simulations and analytic study of the planar state in Hookean sheets. We show that transverse compression is a boundary effect, which originates from the relative extension of the clamped edges with respect to the transversely contracted, compression-free bulk of the sheet, and draw analogy between this edge-induced compression and Moffatt vortices in viscous, cavity-driven flow. Next, we address the instability of the planar state and show that it gives rise to a buckling pattern, localized near the clamped edges, which evolves—upon increasing the tensile load—to wrinkles that invade the uncompressed portion of the sheet. Crucially, we show that the key aspects of the process—from the formation of transversely compressed zones, to the consequent instability of the planar state and the emergence of a wrinkle pattern—can be understood within a Hookean framework, where the only origin of nonlinear response is geometric, rather than a non-Hookean stress—strain relation.

1 Introduction

Published online: 06 July 2021

A familiar, yet quite nontrivial pattern formation phenomenon, is the parallel array of wrinkles that extend throughout a ribbon—a thin, rectangular-shaped solid sheet—upon pulling its clamped edges apart (Fig. 1a) [1,2]. Recalling that buckling and wrinkling of a thin solid body emerge in response to compression, one may readily conclude that the visible array of wrinkles parallel to the stretching axis, \hat{x} , is due to a compressive component of the stress tensor, along the transverse axis, \hat{y} . However, while a transverse contraction (i.e., negative strain, $\varepsilon_{yy} < 0$) in response to longitudinal tension, $\sigma_{xx} \approx T > 0$, is the essence of the classical Poisson effect, the appearance of transverse compression (i.e., $\sigma_{yy} < 0$) is far less obvious. Indeed, if the pulled edges were not clamped, the whole sheet would have contracted uniformly in the transverse direction, the stress would have been perfectly uniaxial and tensile everywhere (i.e., $\varepsilon_{yy} \propto -\nu T$, where ν is the Poisson ratio, and $\sigma_{xx} = T$, $\sigma_{yy} = \sigma_{xy} = 0$), and the planar, unwrinkled state, would have been stable. Hence, the emergence of transverse compression is necessarily a boundary effect, which may exist only near the clamped edges. While numerical and analytical studies of the planar (unwrinkled) state did reveal the presence of zones with small transverse compression close to the clamped edges [1,3], the physical mechanism underlying this boundary effect remains elusive.

Even more puzzling than the mere existence of transversely compressed zones in the planar state is the ensuing elastic instability. Rather than forming a buckling pattern, characterized by a thickness-independent topography that relieves the transverse compression, the stretched sheet appears to develop a highly corrugated topography, whereby the characteristic wavelength λ of transverse undulations has been reported to be proportional to the square root of the sheet's thickness t [2]. Elastic instabilities of thin bodies that give rise to a thickness-dependent wavelength, $\lambda \sim t^{\alpha}$ (with $\alpha > 0$) are often called "wrinkling" and are known to occur in supported sheets subjected to uniaxial compression, whereby the resistance of the attached subphase to deformation competes with the tendency of the sheet to minimize bending energy¹. For instance, the undulation wavelength of uniaxially compressed solid

 $^{^1}$ "buckling" is thus understood as a particular instance of "wrinkling," where the power $\alpha=0.$



 $^{^{}a}$ e-mail: bdavidov@physics.umass.edu (corresponding author)

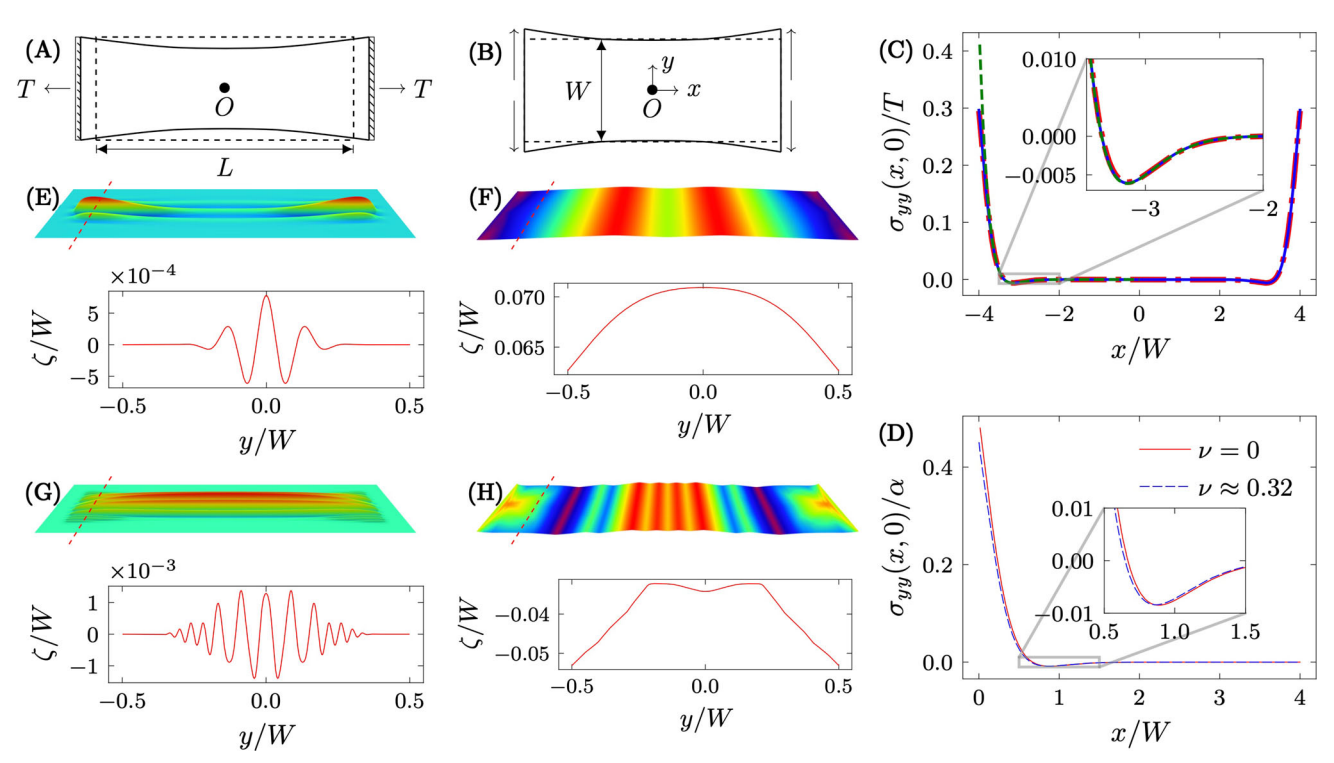


Fig. 1 a Schematic drawing of "model A": a rectangular sheet with width W and length L, subjected to longitudinal tensile loads, T (force/length) that pull on the two short edges, $x = \pm L/2$, while the long edges are free. The short edges are clamped, such that both normal (out-ofplane) displacement, $\zeta(x = \pm L/2, y)$, and transverse (inplane) displacement, $u_y(x = \pm L/2, y)$, vanish, and their longitudinal displacements are $u_x(x = \pm L/2, y) \approx \pm \tilde{T}L/2$. b Schematic drawing of "model B": a similar sheet is subjected to uniform stretching of its two short edges, such that $\partial_y \mathbf{u}_y(x=\pm L/2,y)=\alpha$, while $\zeta(x=\pm L/2,y)=\mathbf{u}_x(x=y)$ $\pm L/2, y) = 0$. c The transverse component of the planar stress, evaluated from our SE simulations along the midline, $\sigma_{yy}(x, y = 0)$, of the stretched sheet (model A, dasheddotted red curve) and the corners-pulled sheet (model B, with $\nu_B = 0$, solid blue curve). Also plotted is the analytic solution (dashed green). The transverse stress profile exhibits a non-monotonic profile, whereby each of the edges at $x = \pm \frac{1}{2}L$ is under transverse strain $((1 - \nu_A \tilde{T}))$ in model A, and $\alpha = (1 - \nu_A \tilde{T})$ in model B), and two corresponding transversely compressed zones whose extent and distance from these edges $\sim W$. The level of the transverse

compression is small, but nonetheless finite fraction of the transverse tension at the edge (the maximal compression is $-\sigma_{yy}(\pm \frac{1}{2}L \mp x_{max}, y = 0) \approx 0.005T$, where $x_{max} \approx 1.5W$). d A plot analogous to c for the corners-pulled sheet (model B) but with Poisson ratio $\nu_B = \nu_A$ (red) rather than $\nu_B = 0$ (dashed blue) exhibits an almost indistinguishable profile of the transverse stress. e-f The deformation $\zeta(x,y)$ of the stretched sheet (model A, in panel E) and the corners-pulled sheet (model B, in panel F) in the nearthreshold regime, $\tilde{T} \approx 2\tilde{T}_c(\epsilon)$. For each model we show a topographic map and a corresponding transverse cross section, $\zeta(x=\frac{1}{2}L-x_{max},y)$. **g-h** Deformation patterns analogous to (E-F), but in the far-from-threshold regime, $\tilde{T} \approx 118 \tilde{T}_c(\epsilon)$. The deformation in Model B, shown in **f** and h, features undulations in the longitudinal direction in addition to transverse buckling, indicating that the longitudinal stress component σ_{xx} is slightly compressive in this case. One may attribute this to Poisson effect, whereby the net tensile load required to pull the corners transversely apart implies small longitudinal confinement, which is eventually relieved by buckling along the \hat{x} -axis

sheets that are floating on a liquid bath or attached to a compliant elastic medium scale as $\lambda \sim t$, and $\lambda \sim t^{3/4}$, respectively [4,5]. However, why does the transverse compression of a suspended sheet give rise to a highly curved wrinkle pattern, $\lambda \sim t^{1/2}$, whose bending energy is substantially larger than a buckling pattern ($\lambda \sim t^0$) that is also capable of relieving transverse compression?

Realizing that the observed wrinkle pattern in this system cannot be described through a standard "post-buckling" approach, in which the out-of-plane deflection of a (naturally planar) sheet is assumed to affect only slightly the planar stress, Cerda and Mahadevan

(CM) proposed to address the system in a strictly distinct, "far from threshold" (FT) regime, $T \gg T_c$, where T_c is a threshold value, below which the compressed planar state is stable [6]. In this approach, which is based on "tension field theory" [7–11], the wrinkle pattern is assumed to be fully developed throughout the whole sheet, and cannot be described as a perturbation to the compressed planar stress, but rather to a compression-free stress field, attained by a hypothetic sheet, with finite stretching modulus and no bending modulus. The CM model inspired a multitude of experimental and theoretical works that addressed the far-from-threshold



regime of wrinkle patterns in various systems of ultrathin sheets subjected to confinement by capillary effects or other forces [12,13]. However, the ingenuous proposal to focus on the FT parameter regime evades some of the basic puzzles exhibited by the system (Fig. 1a) that was the original object of the CM model. Specifically—what is the origin of transversely compressed zones underlying the instability of the planar state? why the out-of-plane deflection of the sheet does not remain localized to these near-edge zones but develops instead into a pattern of small wrinkles that permeate the uncompressed bulk?

In this paper and a subsequent one we revisit the uniaxial stretching of a Hookean ribbon-shaped sheet with clamped edges, and address the planar state, its instability, and the transition from the near threshold regime, $T \gtrsim T_c$, to the far-from-threshold regime, $T \gg T_c$. A primary tool that we employ in our studies is numerical simulations with Surface Evolver (SE) [14], which we find to be an excellent method for finding the planar state as well as the energetic minimum of fully developed wrinkled states in the far-from-threshold regime of very thin sheets. Our rationale in focusing on Hookean elasticity (i.e., a linear stress-strain relationship) is twofold. First, despite the practical importance of effects associated with non-Hookean response, most notably the re-stabilization of a planar, unwrinkled state when the imposed tensile strain is sufficiently large (0.3-0.5 [3,15-20]), the Hookean response unravels the universal (i.e., material-independent) mechanism through which transverse compression emerges and wrinkles develop. Second, since the instability threshold T_c vanishes rapidly with the sheet's thickness (more precisely, T_c vanishes with thickness t faster than the stretching modulus), Hookean mechanics is expected to govern for sufficiently thin sheets not only the transversely compressed planar state and its instability, but also the fully developed wrinkle pattern in the far-from-threshold regime, $T \gg T_c$. The focus of this paper is the planar stress and the characterization of its instability. In the subsequent article we address the evolution of this instability from the near-threshold regime to a fully developed wrinkle pattern in the farfrom-threshold regime.

Starting in Sect. 2 with numerical and analytical study of the planar state, we show that the ultimate cause of transverse compression is the extension of the clamped edges relative to the transversely contracted bulk of the sheet. We elucidate this subtlety by analyzing a specific set-up (model B in Fig. 1) and demonstrate how transverse compression in a rectangular sheet with free long edges can occur even without exerting longitudinal tensile load. In Sect. 3 we address the instability of the planar stress and show that it is essentially an Euler buckling, whose spatial extent is restricted to the transversely compressed zones of the sheet. A direct corollary of this observation is that the emergence of wrinkles in this set-up, whereby the wavelength vanishes with the thickness of the sheet, does not occur at the near-threshold regime $(T \gtrsim T_c)$; instead, it may only be observed in the far-from-threshold regime,

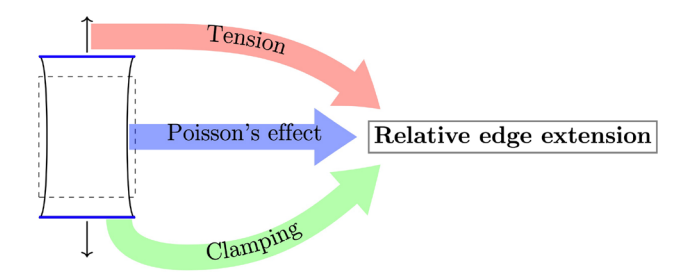


Fig. 2 The identical transverse stress profile in model A and model B indicates that the ultimate cause for a transversely compressed zone in the planar state is a relative extension of the short edge with respect to the bulk. This may be a direct outcome of pulling the short edge outward (model B) or the collective effect of imposing longitudinal tension, clamping the short edge, and positive Poisson ratio (model A)

 $T \gg T_c$. In Sect. 4 we provide evidence for the transition from near-threshold buckling to far-from-threshold wrinkling, and defer an in-depth study of the latter to a subsequent paper.

2 The planar state

The observation that longitudinal tension does not induce transverse compression if the short edges are unclamped (or alternatively if $\nu \leq 0$) suggests that the primal cause for transverse compression is neither uniaxial tension nor positive Poisson ratio, but rather a relative extension of the short edges in comparison to the bulk of the sheet. In order to elucidate this geometrical-mechanical effect, we contrast in this section the planar state of our set-up, hence called "model A" (Fig. 1a), with the planar state of another system, called "model B" (Fig. 1b), in which a relative extension of the edge is imposed directly on a rectangular sheet, with arbitrary Poisson ratio and no longitudinal tension.

2.1 Displacement, strain, and Hookean mechanics

Since our focus here is on small strains we express the components of the strain tensor u_{ij} through derivatives of the displacement field, whose in-plane components are u_x, u_y and whose out-of-plane component is ζ :

$$u_{xx} = \partial_x u_x + \frac{1}{2} (\partial_x \zeta)^2 \; ; \; u_{yy} = \partial_y u_y + \frac{1}{2} (\partial_y \zeta)^2 \; ;$$

$$u_{xy} = \frac{1}{2} (\partial_x u_y + \partial_y u_x + \partial_y \zeta \partial_x \zeta) \; , \tag{1}$$

and invoke the Hookean stress–strain relationship [21]:

$$\sigma_{xx} = \frac{1}{1-\nu^2} Y(u_{xx} + \nu u_{yy}) ; \sigma_{yy} = \frac{1}{1-\nu^2} Y(u_{yy} + \nu u_{xx}) ;$$

$$\sigma_{xy} = \frac{1}{1+\nu} Y u_{xy} .$$
 (2)

The two problems we address in this section, "model A" and "model B," are defined below through suitable



boundary conditions (BCs) on the stress tensor and the displacement field. Since we consider only small strains, we employ the standard approach of Hookean elasticity theory, and assume the BCs hold at the edges of the original, undeformed sheet, namely the long edges $y=\pm\frac{1}{2}W$ and the short edges $x=\pm\frac{1}{2}L$.

In analyzing the planar state we consider a displacement field with $\zeta = 0$. A useful tool for this analysis is the Airy potential – a scalar function $\Phi(x, y)$ such that:

$$\sigma_{yy} = \frac{\partial^2 \Phi}{\partial x^2} \; ; \; \sigma_{xx} = \frac{\partial^2 \Phi}{\partial y^2} \; ; \; \sigma_{xy} = -\frac{\partial^2 \Phi}{\partial x \partial y} \; .$$
 (3)

The mechanical equilibrium equation, $\partial_j \sigma_{ij} = 0$, becomes the bi-harmonic equation for the Airy potential:

$$\nabla^4 \Phi = 0 \ . \tag{4}$$

2.2 Model A versus model B

The mathematical description of our original set-up ("model A," Fig. 1a) consists of a non-homogeneous BC:

$$\int_{-\frac{W}{2}}^{\frac{W}{2}} \sigma_{xx}(x = \pm \frac{1}{2}L, y) dy = TW,$$
 (5a)

expressing the fact that a force TW is pulling each of the short edges outward (and applies also for any $-\frac{1}{2}L \leq x \leq \frac{1}{2}L$ by force balance consideration). Additionally, there are four homogeneous BCs:

at
$$y = \pm \frac{1}{2}W$$
: $\sigma_{yy} = \sigma_{xy} = 0$ (5b)

at
$$x = \pm \frac{1}{2}L$$
: $u_y = 0$; $\frac{\partial u_x}{\partial y} = 0$. (5c)

The first two Eq. (5b) reflect the fact that the long edges are free, namely $\sigma_{ij}n_j=0$, where $\hat{n}=\pm\hat{y}$ is the outward normal to the long (undeformed) edges, respectively. The last two Eq. (5c) imply that the short edges are displaced as rigid, inextensible sticks, pulled apart along the \hat{x} -axis, such that their displacement is given by $u_x=Const$ and $u_y=0$.

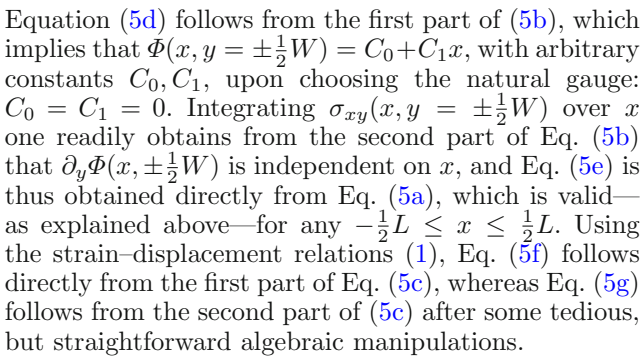
With the aid of Eq. (3) the BCs (5a, 5b, 5c) may be converted to a set of four BCs for the Airy potential:

at
$$y = \pm \frac{1}{2}W$$
: $\Phi = 0$ (5d)

and
$$\frac{\partial \Phi}{\partial y} = \pm \frac{1}{2}TW$$
 (5e)

at
$$x = \pm \frac{1}{2}L$$
: $\frac{\partial^2 \Phi}{\partial x^2} - \nu \frac{\partial^2 \Phi}{\partial y^2} = 0$ (5f)

and
$$\frac{\partial^3 \Phi}{\partial x^3} + (2+\nu) \frac{\partial^3 \Phi}{\partial x \partial y^2} = 0$$
. (5g)



Turning now to "model B" (Fig. 1b), we describe the BCs in analogous manner to Eq. (5). First, the absence of exerted tension along the \hat{x} -axis implies that:

$$\int_{-\frac{W}{2}}^{\frac{W}{2}} \sigma_{xx}(x = \pm \frac{1}{2}L, y) dy = 0,$$
 (6a)

(as well as for any $-\frac{1}{2}L \leq x \leq \frac{1}{2}L$). Second, three BCs are identical to their homogeneous counterparts in model A:

at
$$y = \pm \frac{1}{2}W$$
: $\sigma_{yy} = \sigma_{xy} = 0$ (6b)

at
$$x = \pm \frac{1}{2}L$$
: $\frac{\partial u_x}{\partial y} = 0$, (6c)

whereas the last BC is non-homogenous

at
$$x = \pm \frac{1}{2}L$$
: $\frac{\partial u_y}{\partial y} = \alpha$ (6d)

such that $\alpha>0$ is a transverse strain imposed directly at the short edges. The conversion of the BCs (6a–6d) into BCs for the Airy potential proceeds along the same steps that led from Eqs. (5a–5c) to Eqs. (5d–5g), yielding:

at
$$y = \pm \frac{1}{2}W$$
: $\Phi = 0$ (6e)

and
$$\frac{\partial \Phi}{\partial y} = 0$$
 (6f)

at
$$x = \pm \frac{1}{2}L$$
: $\frac{\partial^2 \Phi}{\partial x^2} - \nu \frac{\partial^2 \Phi}{\partial y^2} = \alpha Y$ (6g)

and
$$\frac{\partial^3 \Phi}{\partial x^3} + (2+\nu) \frac{\partial^3 \Phi}{\partial x \partial y^2} = 0.$$
 (6h)

Note that the planar stress of a Hookean sheet is determined by a purely linear problem, namely both the strain–displacement relation (1) and the stress–strain relation (2) are given by linear equations, and consequently the stress, strain, and displacement fields for each of the two models are fully determined by solving a linear PDE (4) subjected to the corresponding BCs [Eqs. (5a–5g) for model A or Eqs. (6a–6h) for model B]. Furthermore, each of the two models consists of a single non-homogeneous BC [Eq. (5a) for model A and Eq. (6d) for model B], and therefore the stress field in



² The error incurred by considering BCs through the undeformed, rather the deformed sheet, is a higher order in T/Y.

model A:
$$\sigma_{ij}(x, y; T_2) = \frac{T_2}{T_1} \sigma_{ij}(x, y; T_1)$$

model B: $\sigma_{ij}(x, y; \alpha_2) = \frac{\alpha_2}{\alpha_1} \sigma_{ij}(x, y; \alpha_1)$ (7)

2.3 Numerical simulations

We employ SE to study the planar state of the two models, implementing an equilateral-triangular mesh of density 6.95×10^5 (total area/cell area). The SE builtin "linear_elastic" method is adapted for computing the strain energy, and "star_perp_sq_mean_curvature" and "star_qauss_curvature" to compute bending energy.

For model A, we consider a sheet with a relatively large length-to-width ratio, $\frac{L}{W}=8$, a Poisson ratio $\nu_A=0.32$, and some exerted longitudinal tension Twhose actual numerical value is arbitrary [see Eq. (7)]. For model B, we consider a sheet with the same lengthto-width ratio, $\frac{L}{W} = 8$, and Poisson ratio $\nu_B = \nu_A$ or $\nu_B = 0$. Since in model B $u_{yy} = 0$ in the bulk, we make the extension of the short edge relative to the bulk identical to model A (where $u_{yy} = 0$ at the clamped edge and $-\nu_A T/Y$ in the bulk), by choosing the edge extension parameter in model B to be $\alpha = \nu_A T/Y$.

While the longitudinal stress components, $\sigma_{xx}(x,y)$, of the two models are obviously distinct, Fig. 1c, d show that the transverse stress, $\sigma_{yy}(x,y)$ in the two models is essentially identical. Furthermore, the direct effect of the Poisson ratio is negligible, as can be seen by comparing the transverse stress of model B with $\nu_B =$ ν_A and $\nu_B = 0$. As Fig. 1c, d show, the transverse stress is positive (tensile) in the vicinity of the short edges, becoming compressive at a distance $\approx 1.5 \cdot W$ from each short edge, and remains compressive over a strip of length $\sim W$, after which it vanishes exponentially.

Our numerical solution of the planar stress in the two models indicates that the essential cause of transverse compression in a rectangular sheet is the extension of the short edge relative to the bulk. As the schematic in Fig. 2 shows, this effect can be attained directly (as is the case in model B) even for a sheet with $\nu = 0$ with no longitudinal tensile load, or indirectly—as in our original model A—by applying longitudinal tension and clamping the short edges of a sheet with positive Poisson ratio.

2.4 Analytical solution

2.4.1 Equivalence of model A and model B

The identity of the transverse stress components in models A and B can be understood by decomposing the Airy potential of model A into "bulk" and "edge" terms:

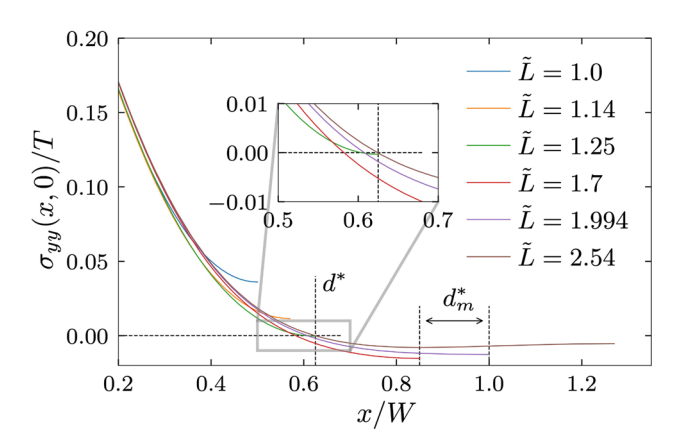


Fig. 3 Our SE simulations of the planar state in Hookean sheets with various aspect ratios, $\tilde{L} = L/W$. In order to conveniently show the values of d^* and d_m^* , we shift the x-axis, $x \to x + \frac{L}{2}$, such that the left clamped boundary (not shown) is at x = 0, and show only the left half of the sheet. The transverse stresses of different L/W suggest the existence of a parameter regime (i) where the stress may be purely tensile and the planar state is thus stable $(\frac{L}{W} < 2d^*)$; (ii) where transverse compression exists around the middle of the sheet $(2d^* < \frac{L}{W} < 2d_m^*)$; and (iii) where transverse compression exists in two zones $(\frac{L}{W} > 2d_m^*)$. For d^* , the numerical value extracted from our SE simulations is $d^* \approx$ 0.625, whereas for d_m^* the extracted value is $d_m^* \approx 0.8$ – 1.0 (the uncertainty is a consequence of a very shallow local maximum of $\sigma_{yy}(x,0)$.)

model A:
$$\Phi(x,y) = \Phi_b(x,y) + \Phi_e(x,y)$$

where: $\Phi_b(x,y) = \frac{1}{2}T(y^2 - 1)$. (8a)

If the short edges were not clamped (i.e., if the first part of Eq. (5c) had been replaced by $\partial_y^2 u_y = 0$, such that $u_{yy}(x=\pm \frac{1}{2}L,y)$ may be nonzero), then $\Phi_e=0$, and the resulting stress, associated only with Φ_b , would have been constant: $\sigma_{xx} = T$, $\sigma_{yy} = \sigma_{xy} = 0$. However, clamping implies that $\Phi_e(x,y) \neq 0$, since it must satisfy the non-homogenous set of BCs:

at
$$y = \pm \frac{1}{2}W$$
: $\Phi_e = 0$ (8b)

and
$$\frac{\partial \Phi_e}{\partial y} = 0$$
 (8c)

and
$$\frac{\partial \Phi_e}{\partial y} = 0$$
 (8c)
at $x = \pm \frac{1}{2}L$: $\frac{\partial^2 \Phi_e}{\partial x^2} - \nu_A \frac{\partial^2 \Phi_e}{\partial y^2} = \nu_A T$ (8d)

and
$$\frac{\partial^3 \Phi_e}{\partial x^3} + (2 + \nu_A) \frac{\partial^3 \Phi_e}{\partial x \partial y^2} = 0.$$
 (8e)

Remarkably, the BCs (8b–8e) are identical to the BCs satisfied by the Airy potential $\Phi(x,y)$ of model B (6e– 6h), with $\nu_B = \nu_A$, and edge extension $\alpha = \nu_A T/Y$! This observation immediately explains our numerical result: the planar stress field of the original problem (model A) is identical (up to a constant, purely uniaxial stress, $\sigma_{xx} = T, \sigma_{yy} = \sigma_{xy} = 0$) to the stress field in a sheet whose short edges are pulled outward, and no longitudinal tension.



2.4.2 The origin of transverse compression

The above discussion reveals that the origin of transverse compression in a longitudinally stretched sheet whose short edges are clamped is the "edge-induced" potential $\Phi_e(x,y)$ in decomposition (8a), or equivalently the Airy potential of our model B. It is thus natural to seek a solution using a basis of eigenfunctions of the bi-harmonic equation:

$$\Phi^{i,c}(x,y) = e^{-p_i \frac{x}{W}} \cos\left(p_i \frac{y}{W}\right) ,$$

$$\Phi^{i,s}(x,y) = e^{-p_i \frac{x}{W}} \frac{y}{W} \sin\left(p_i \frac{y}{W}\right) , \qquad (9a)$$

where $\{p_i\}_{i=1}^{\infty}$ is a discrete set of (generally complex) eigenvalues, which must be determined through the BCs (6e–6h), and the symmetry: $\Phi(x,y) = \Phi(x,-y)$ has been exploited.

Assuming $\{Re\ p_i\} > 0$, the basis functions (9a) describe deformations that decay as $x/W \to \infty$, hence – supplemented by the analogous set of functions $(p_i \to -p_i)$ that describes deformations that decay as $x/W \to -\infty$ —this basis is useful to describe deformations of a very elongated sheet, namely, $L/W \gg 1$. In the following calculation we consider this limit (which may be loosely called an "infinitely long" sheet). Our numerical simulations show that for L/W larger than 3–4, the stress profile is nearly indistinguishable from the one obtained by a calculation based on the basis functions (9a) and the assumption $L/W \gg 1$. Let us consider then -L/2 < x < 0 and express the solution $\Phi_e(x,y)$ through the basis functions (9a):

$$\Phi_e(x,y) = Re\left\{ \sum_i C_i \cdot \left(\Phi^{i,c}(x,y) + A_i \Phi^{i,s}(x,y) \right) \right\},$$
(9b)

In order to determine the eigenvalues $\{p_i\}$ and the sequence of coefficients $\{A_i\}, \{C_i\}$, we must apply the BCs (8b–8e). This is a rather tedious process, which requires an inverse Laplace transform [22], and we thus defer it to an appendix. Nevertheless, it is useful to note that the eigenvalues $\{p_i\}$ are determined by the equation:

$$p_i + \sin p_i = 0 , \qquad (9c)$$

and in turn determine the coefficients $\{A_i\}$ through the simple relation:

$$A_i = -2\cot\frac{p_i}{2} \,\,\,\,(9d)$$

while obtaining the sequence $\{C_i\}$ requires an explicit evaluation of an inverse Laplace transform. The numerical values of $\{|p_i|\}$ and $\{|C_i|\}$ are plotted in Fig. 4 (for $1 \le i \le 20$, where the order is determined by increasing $|p_i|$'s). Remarkably, Eq. (9c) reveals two facts on whose importance we will elaborate below: (a) All eigenvalues

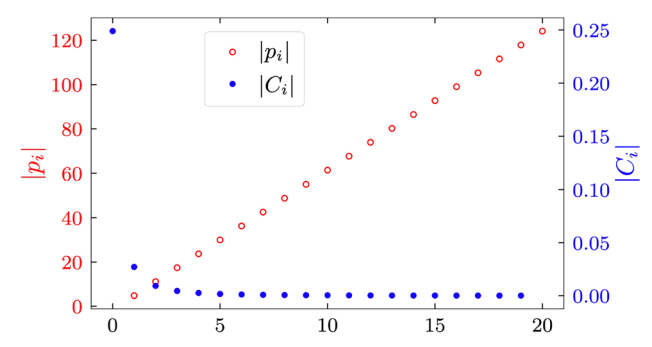


Fig. 4 The magnitudes of the first 20 eigenvalues $|p_i|$ and coefficients $|C_i|$, show that $|p_i|$ increases in constant increments while $|C_i|$ is decreasing quickly, and thus only the leading term contributes significantly to the solution

Table 1 The values of the three leading poles (p_i) , and corresponding pairs of coefficients (A_i, C_i) in the expansion, Eq. (9b), for the Airy function

	p_i	A_i
i = 1	4.212 + 2.251j	0.332 + 1.78j
i = 2	10.713 + 3.103j	0.168 + 1.94j
$\underline{i=3}$	17.073 + 3.551j	0.111 + 1.97j
	$\nu_B = 0.32 \; (\times 10^{-3})$	$\nu_B = 0 \; (\times 10^{-3})$
C_1	109 - 213j	131 - 229j
C_2	-22.9 + 13.5j	-26.1 + 11.7j
C_3	8.68 - 2.84j	9.49 - 1.52j

The values of the coefficients C_i are normalized by the edge extension α (model B) or $\nu_A T/Y$ (model A). Note that the poles p_i and coefficients A_i are independent on the Poisson ratio

 p_i are non-real numbers. (b) the eigenvalues p_i and the coefficients A_i do not depend on the Poisson ratio ν_B , and approach a well-defined limit values as the length-to-width ratio $\frac{L}{W} \to \infty$.

In Table 1 we report the values of the three eigenvalues p_i with the smallest (positive) real parts, which govern sum (9b), together with the corresponding values of A_i and C_i . Note that C_i is proportional to α , so that upon normalizing by α they depend only on the Poisson ratio.

Figure 1c, d show that approximating the Airy potential through the first term in sum (9b), i.e.,

$$\Phi_{e}(x,y) \approx \operatorname{Re}\left\{C_{1}e^{-p_{1}\frac{x}{W}}\left[\cos\left(p_{1}\frac{y}{W}\right)\right] -2\cot\left(\frac{p_{1}}{2}\right)\frac{y}{W}\sin\left(p_{1}\frac{y}{W}\right)\right]\right\}, \qquad (9e)$$

matches already very well the transverse stress obtained in the numerical solution at the vicinity of the short edges of a sheet with $\frac{L}{W} = 8$. Furthermore, the analytic solution of the edge-induced Airy function $\Phi_e(x, y)$, given by Eq. (9b) with the numerical values of $\{p_i, A_i, C_i\}$ in Table 1, provides some valuable insights



into the mechanism by which transverse compression develops in an elongated sheet.

- First, Table 1 indicates that the dependence on Poisson ratio, which stems only from the sequence $\{C_i\}$, is very weak. This observation, which has been noted already in our numerical analysis, substantiates the rationale illustrated in Fig. 2—the primary cause of transverse compression is the extension of the short edges relative to the bulk, rather than the Poisson ratio of the sheet.
- Second, the unavoidable presence of transversely compressed zone in a sufficiently long sheet is a direct consequence of the fact that all eigenvalues $\{p_i\}$, namely roots of Eq. (9c), are complex. The implication is revealed by evaluating σ_{yy} from the approximated Airy potential (9e) along the centerline (y = 0) of a semi-infinite sheet:

$$\sigma_{yy}(x, y = 0) \propto e^{-p_1^{(r)} \cdot \frac{x}{W}} \cos[p_1^{(i)} \cdot \frac{x}{W} + g] ,$$

$$g = \tan^{-1} \left(\frac{C_1^{(i)} p_1^{(r)^2} + 2C_1^{(r)} p_1^{(i)} p_1^{(r)} - C_1^{(i)} p_1^{(i)^2}}{C_1^{(r)} p_1^{(i)^2} + 2C_1^{(i)} p_1^{(i)} p_1^{(r)} - C_1^{(r)} p_1^{(r)^2}} \right)$$

$$(9f)$$

where the superscripts $^{(i)}$ and $^{(r)}$ refer to the imaginary and real parts, respectively. It is evident from the first line of Eq. (9f) that the imaginary component of the root, $p_1^{(i)} \neq 0$, gives rise to negative (i.e., compressive) transverse stress at $-\frac{1}{2}L + d^*W < x < -\frac{1}{2}L + d^*_mW$ and $\frac{1}{2}L - d^*_mW < x < \frac{1}{2}L - d^*W$, where:

$$d^* = (\pi/2 - g)/p_1^{(i)} \approx 0.646$$

$$d_m^* = d^* + \tan^{-1}(p_1^{(i)}/p_1^{(r)})/p_1^{(i)} \approx 0.864 . \quad (9g)$$

- \bullet Third, Eq. (9g), indicates that the response of a rectangular sheet whose short edges are extended relative to the bulk, can be classified into three types, depending solely on the aspect ratio, $\frac{L}{W}$:
- (I) For $\frac{L}{W} < 2d^*$ there is no transverse compression. Here, the transverse stress, which is obviously tensile at the far edges $(x = \pm \frac{1}{2}L)$, does not have enough room to vary significantly, hence the whole sheet is under pure (biaxial) tension.
- (II) For $2d^* < \frac{L}{W} < 2d_m^*$ there is a single transversely compressed zone located around the center of the sheet. Here, the sheet is sufficiently elongated such that the transverse stress has enough room to approach negative values away from the tensed edges, but not to overturn and decay to zero. Hence, the two compressive zones, generated by each of the tensed edges, are merged into a single one.
- (III) If $\frac{L}{W} > 2d_m^*$ the sheet is long enough such that there are two transversely compressed zones, each of them starts at a distance d^*W from a tensed edge, and extends over a length $\propto W$. We note that since the eigenvalue p_1 is complex, the Airy potential $\Phi_e(x,y)$, Eq. (9e), gives rise to additional transversely compressed zones, away from the clamped edges. However,

the exponential decay of $\Phi_e(x,y)$ with the corresponding distance $(|x\pm L/2|)$ implies that the magnitude of compression in these zones is much smaller in comparison to the transverse compression in the first zone. Since the stability of the planar state to buckling is determined by the maximal compression, these additional compressive zones have thus little effect on the mechanics.

Figure 3 shows the transverse stress profile, obtained from our simulations for several representative values of the aspect ratio L/W, supporting the above classification into three regimes. We note that the actual values of d^* and d_m^* obtained from our simulations are rather close, but not identical, to the theoretical prediction, Eq. (9g). An obvious reason for this discrepancy is that the values of d^*, d_m^* , reported in Eq. (9g), are obtained from an analytic solution of the transverse stress in a semi-infinite sheet (i.e., $\frac{L}{W} \to \infty$), and we may thus expect corrections of $O(\frac{W}{L})$ to this predictions. From this viewpoint, Fig. 3 indicates that those corrections are in fact surprisingly small. Thus, while the above classification has been noted before by numerous workers (e.g., [3]), our analytic approach elucidates the origin of this classification through the complex values of the eigenvalues $\{p_i\}$ of the bi-harmonic equation under the BCs (8a).

• Finally, we note that employing the basis functions (9a) yields a rapidly converging sequence and thereby the compact expression (9e) that describes quantitatively the stress field throughout the whole sheet. This global approach, which has been employed broadly for solving the bi-harmonic equation in viscous fluid mechanics and linear elasticity problems [22,23] is thus advantageous to an approximation using "corner functions" [24] that does not explain the emergence of transverse compression.

2.4.3 Analogy to Moffatt eddies in a "driven cavity" flow

We have seen that the existence of complex eigenvalues of the bi-harmonic equation (4) for the edge-induced Airy potential Φ_e gives rise to a non-monotonic transverse stress $\sigma_{yy} = \partial_{xx} \Phi_e$, and consequently to transversely compressed zones. It is useful to point out an analogy between this (arguably non-intuitive) effect and a classical phenomenon in fluid mechanics, known as "Moffatt eddies" [25]. Considering a class of twodimensional (2D) viscous flows generated by the motion of rigid boundaries, Moffatt showed that solutions of the bi-harmonic equation, which describes the stream function of 2D Stokes flows, may be characterized by complex eigenvalues. A notable implication of this basic observation is the emergence of eddies in the "drivencavity" set-up, whereby a rigid plate is moving at a constant velocity, dragging the surface of a viscous fluid enclosed in a deep cavity [26] (Fig. 5). The formation of these eddies is intimately related to the complex eigenvalues that govern the stream function. The real (negative) part of the eigenvalues reflects the intuitive fact that the magnitude of the viscous stress (and conse-



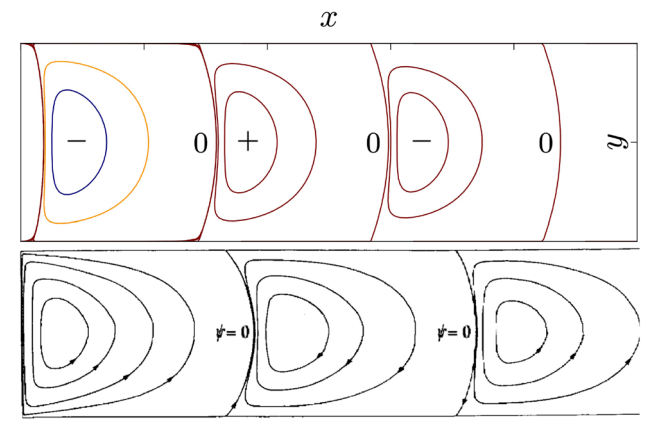


Fig. 5 Top: Contour plot of Airy potential Φ that describes the planar stress in a semi-infinite Hookean strip (9e). The symbols "+" and "–" indicate the sign of Φ . Bottom: Moffatt eddies structure in a 2D Stokes flow in a driven rectangular cavity [26]. The viscous stress (and consequently the velocity field) in an incompressible Newtonian fluid is derived from a stream function that satisfies the bi-harmonic equation, similarly to the way by which the elastic stress in a solid Hookean sheet is derived from the Airy potential.

quently the speed) decays away from the driven surface, whereas the imaginary part implies that the decaying stress is nevertheless non-monotonic, and consequently an alternating direction of the velocity.

Thus, the transverse compression induced in a solid sheet by a relative extension of an edge with respect to the bulk may be viewed as an "elastic analog" of Moffatt eddies in a 2D driven-cavity viscous flow, providing a notable example of the Stokes–Rayleigh analogy between the mechanical equilibrium of Hookean solids and the viscous flow of Newtonian fluids.

3 Buckling instability

When subjected to compressive loads, slender solid bodies become unstable, "trading" a highly energetic strain (averaged through the body's cross section), which is penalized by the stretching modulus Y, with curvature of the body's mid-plane, which is penalized by the bending modulus, $B \sim Yt^2$. The primary question we seek to address here is how the instability mode and the threshold value of the control parameter (longitudinal tension T in model A and edge extension α for model B) depend on the sheet thickness t.

Before studying this instability in our problem, where the planar stress is nonuniform (Figs. 1c, d, 3), it is useful to recall the basic example of a rectangular sheet under uniaxial compressive load (Fig. 6), where the planar stress is uniform and purely compressive $(\sigma_{yy} = -\sigma_0 < 0, \sigma_{xx} = \sigma_{xy} = 0)$.



The most elementary type of an elastic instability under a uniform uniaxial compressive load, $\sigma_{uu} = -\sigma_0$, is exhibited by an unsupported rectangular sheet, of thickness t and width W, whose edges, $x=\pm \frac{1}{2}\ell$, are free (Fig. 6a). In a popular explanation of this instability, known as "Euler buckling," the deflected state of the sheet is modeled as an Euler *elastica*—a strainless deformation that fully converts compression into out-ofplane deflection—and its bending energy ($\propto B \frac{\sigma_0}{V} \frac{1}{W^2}$) is compared with the strain energy of the planar state $(\propto \frac{\sigma_0^2}{V})$. We note, however, that this common explanation is a "far from threshold" reasoning, which does not capture the physics at the vicinity of a continuous (supercritical) bifurcation. Instead, we provide here another explanation for the Euler instability, addressing it as one that emerges from a standard supercritical bifurcation, in accord with the near-threshold analysis that is the focus of the current paper.

Consider then some given value of σ_0 , and assume an undulatory deviation $\zeta(x,y) = A \cdot g_{\lambda}(y)$ from the planar state, where the amplitude A is infinitesimal, and $g_{\lambda}(y)$ is some function that undulates over a scale λ . Generally, $g_{\lambda}(y)$ is an eigenfunction of the elastic energy functional, linearized around the planar state, and for this highly symmetric problem it is simply sinusoidal. Nevertheless, we prefer to keep a more general terminology in order to highlight the commonality with our original model problem, which is far less symmetric. Such a perturbation reduces slightly the strain in the planar state: $\varepsilon_{yy} \to -\frac{\sigma_0}{Y} + C_1 \cdot (\frac{A}{\lambda})^2$, where $C_1 > 0$ is some numerical constant. For an infinitesimal A, the strain energy is reduced (from the planar-state) by a value $\propto \sigma_0(\frac{A}{\lambda})^2$, whereas the bending energy (which is obviously zero at the planar state) is increased by a value $\propto B(\frac{A}{\lambda^2})^2$, and one readily finds that such a perturbation of the planar state becomes favorable once the compressive load exceeds a threshold, $\sigma_0^*(\lambda) \sim B/\lambda^2$. Since the wavelength λ is limited by the width W, we find that the planar state first becomes unstable to undulations at the largest possible wavelength, when the exerted compressive load exceeds a threshold value, $\sigma_c = \sigma_0^*(W)$:

Euler buckling:
$$\sigma_c \sim \frac{B}{W^2} \sim Y \left(\frac{t}{W}\right)^2$$
; $\lambda \sim W$. (10)

Let us consider now two other variants of the instability under uniform, uniaxial compressive load. The first variant, known as the Winkler model and depicted in Fig. 6b, consists of a sheet attached to an elastic substrate, which penalizes vertical displacement by an energy (per area), $\frac{1}{2}K_{\rm sub}\zeta^2$. The additional energy cost for undulations implies that, for a given λ , a planar state becomes unstable only if σ_0 exceeds an enhanced threshold value, $\sigma_0^*(\lambda) \sim B/\lambda^2 + K_{\rm sub}\lambda^2$. Consequently, we find that the planar state first becomes unstable to undulations at a wavelength, $\lambda_c \sim (B/K_{\rm sub})^{1/4}$, which may be $\ll W$, when the exerted compressive load exceeds a threshold value, $\sigma_c \sim \sqrt{BK_{\rm sub}} \sim \sqrt{YK_{\rm sub}} \cdot t$.



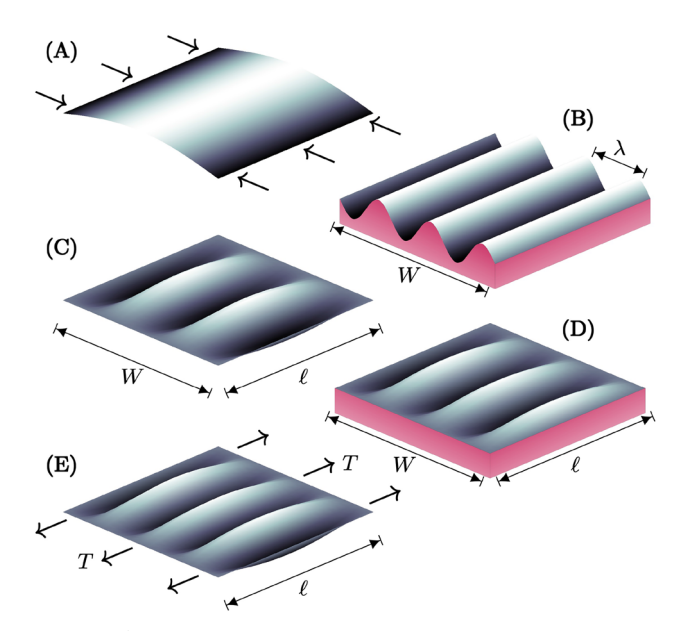


Fig. 6 A schematic of a rectangular sheet under uniaxial compressive load, $\sigma_{yy} = -\sigma_0$. a A classic version of the Euler buckling instability, where the edges, $x = \pm \ell/2$, are free, and the unstable mode consists of a single undulation $(\lambda \sim W)$, regardless of the length ℓ . **b** Attachment to an elastic substrate ("Winkler foundation") of stiffness $K_{\rm sub}$ enhances resistance to undulations and thereby the threshold σ_c , and reducing the wavelength. **c**-**d** If the amplitude is suppressed at the edges $x = \pm \ell/2$, the instability mode is affected by the length ℓ , such that the threshold σ_c is increased in comparison to **a** and the near-threshold undulation wavelength λ_c is decreased. For $\ell \ll W$ the near-threshold pattern consists of periodic undulations of wavelength $\lambda_c \sim \ell$. **e** The presence of longitudinal tension, $\sigma_{xx} = T$, acts as an "effective substrate" of stiffness $K \sim T/\ell^2$ [6], affecting further reduction in the wavelength and correspondingly enhancement of the threshold value σ_c

These two features—a wavelength that exhibits strong dependence on the sheet thickness (i.e., $\lambda \sim t^{\beta_{\lambda}}$ with $\beta_{\lambda} > 0$) and an enhanced threshold for destabilizing a planar state (i.e., $\sigma_c/Y \sim t^{\beta_{\sigma}}$ with $\beta_{\sigma} < 2$) are hallmarks of wrinkling phenomena, demarcating them from the standard version of Euler buckling instability.

A second variant of instability under uniform, uniaxial compressive load, is depicted in Fig. 6c, d. Here, the amplitude is suppressed at the edges $x=\pm\frac{1}{2}\ell$, such that a shape $A\cdot\zeta_\lambda(x,y)$ that undulates over a characteristic scale λ along the compressive axis (\hat{y}) , must vary also along the \hat{x} -axis, thereby being penalized also by the bending cost of the corresponding curvature, $\propto A/\ell^2$. For a given λ , a planar state becomes unstable only if the compressive load exceeds, $\sigma_0^*(\lambda) \sim B(1/\lambda^2 + \lambda^2/\ell^4)$, and if $\ell \ll W$ we find that the planar state first becomes unstable to undulations of wavelength, $\lambda_c \sim \ell$, at a threshold, $\sigma_c \sim B/\ell^2 \sim Y(\frac{t}{\ell})^2$. Furthermore, if the sheet is subjected also to a tensile load $\sigma_{xx} = T$ along the longitudinal (\hat{x}) -axis (Fig. 6e), there will be yet another energetic penalty for undulations,

 $\sim T(\frac{A}{\ell})^2$, which is analogous to the energy implied by an actual (Winkler) substrate, $K_{\text{sub}} \propto T/\ell^2$.

Putting together the effects of a real substrate, amplitude-suppressing boundaries, and longitudinal tension, we find that, for a given wavelength λ , the planar state of a rectangular sheet under uniform compression in the transverse (\hat{y}) -axis becomes unstable if the compressive load σ_0 exceeds:

$$\sigma_0^*(\lambda) \sim B \frac{1}{\lambda^2} + \left(K_{\rm sub} + T \frac{1}{\ell^2} + B \frac{1}{\ell^4} \right) \lambda^2 \ , \ \ (11a)$$

and hence the instability is characterized by a wavelength

$$\lambda_c \sim \min\left(W \; , \; \left(\frac{B}{K_{\text{sub}} + T\ell^{-2} + B\ell^{-4}}\right)^{1/4}\right)$$
(11b)

and occurs as the compressive load exceeds a threshold

$$\sigma_c \sim \max\left(BW^{-2}, \sqrt{B(K_{\text{sub}} + T\ell^{-2} + B\ell^{-4})}\right).$$
 (11c)

3.2 Why is the instability buckling-like?

Let us turn back now to our problem—where the transverse stress induced by the relative edge is nonuniform (Figs. 1c, d, 3), namely $\sigma_{yy}(x,y)$ varies along both \hat{x} and \hat{y} axes. One can still perform a linear stability analysis of the planar stress to infinitesimal deflections, $\zeta(x,y) = A \cdot g_{\lambda}(x,y)$, which undulate with a characteristic wavelength λ along the \hat{y} -axis and an infinitesimal amplitude A. However, the lack of translation symmetry of the planar state implies that the eigenfunctions, $g_{\lambda}(x,y)$, of the corresponding (linearized) energy functional are not simply sinusoidal Fourier modes. Nevertheless, as we explain below the physical mechanisms that determine the critical wavelength λ_c and the threshold σ_c for the uniform compression problem, Eqs. (11a–11c), are analogous to those that govern the instability of the nonuniform planar stress in our problem, allowing us to gain valuable insights.

Let us consider first model B, where the magnitude $\sigma_0 \propto \alpha \cdot Y$ of the transverse compressive stress is induced directly by the edge extension parameter, α , and the stretching modulus Y. Here, there is no longitudinal tension (T=0), and—since our sheet is unsupported (i.e., $K_{\rm sub}=0$)—nor there is a real substrate effect. Since the transverse compression in the planar state is limited to a narrow zone in the sheet, the compressive stress $\sigma_0^*(\lambda)$ above which an undulation of wavelength λ becomes favorable is subjected to the effect of amplitude-suppressing boundaries discussed above (last term in Eq. 11a). However, since the length of the compressive zone is proportional to the sheet's width (i.e., $\ell \propto W$), the overall effect on the critical wavelength λ_c



and threshold value $\sigma_c * \propto \alpha_c Y$ is inconspicuous, and we find the scaling:

model B:
$$\alpha_c \sim \frac{B}{YW^2} \sim \left(\frac{t}{W}\right)^2$$
; $\lambda_c \sim W$. (12)

Turning now to our original problem (model A), where the magnitude of the transverse compressive stress $\sigma_0 \propto T$, we recognize an additional contribution to $\sigma_0^*(\lambda)$, Eq. (11a), due to the energetic cost for deflection over a length $\ell \sim W$ along the tensile axis. However, since σ_0 is also proportional to the longitudinal tension T, we find that the minimal value of T for which Eq. (11a) is satisfied is again realized when the wavelength λ is a finite, thickness-independent fraction of the sheet width, implying:

model A:
$$T_c \sim \frac{B}{W^2} \sim Y \cdot \left(\frac{t}{W}\right)^2$$
; $\lambda_c \sim W$. (13)

Thus, notwithstanding the narrowness of the compressive zone and the presence of longitudinal tension in it, inspection of Eq. (10) and Eqs. (12, 13) reveals that the instability of the planar shape caused by relative edge extension exhibits the typical behavior of the classic Euler buckling instability, namely a thicknessindependent critical "wavelength" λ_c set by the sheet geometry, and a threshold load value that scales as the square power of the thickness-width ratio. An important implication of the analogy $\alpha \leftrightarrow \nu T/Y$ between models A and B, realized by inspecting Eqs. (12) and (13), is that the proportionality constant for T_c in Eq. (13) diverges as $\nu \to 0$. Namely, the ratio between the magnitudes of the transverse and longitudinal stress components (which is generally nonzero near the clamped edges) vanishes as $\nu \to 0$, such that the exerted longitudinal tension needed to trigger a transverse buckling instability diverges in this limit.

Figure 7 shows that the predicted buckling-like behavior, characterized by the scaling rules (12, 13), is confirmed by our simulations. In Fig. 7a, threshold values (T_c for model A and α_c for model B) were obtained for a range of sheet thicknesses by carefully probing intervals of the control parameters (T and α , respectively), and then plotted versus the aspect ratio $\frac{t}{W}$, showing an excellent agreement with the predicted scaling behavior. Apart from their identical scaling behavior, the threshold value of the dimensionless control parameter T_c/Y in model A is larger than its counterpart α_c in model B, in accord with the enhanced resistance of the former to buckling, due to the effect of longitudinal tension in the transversely compressed zone. The enhanced resistance to undulations is reflected also in the near-threshold pattern (Fig. 1e, f). While both models exhibit near threshold a buckling (i.e., thickness-independent undulation) pattern, such that the wavelength λ_c is a finite fraction of the width W, this fraction is smaller in model A (by a factor of $\approx \frac{1}{3}$) in comparison to its counterpart in model B.

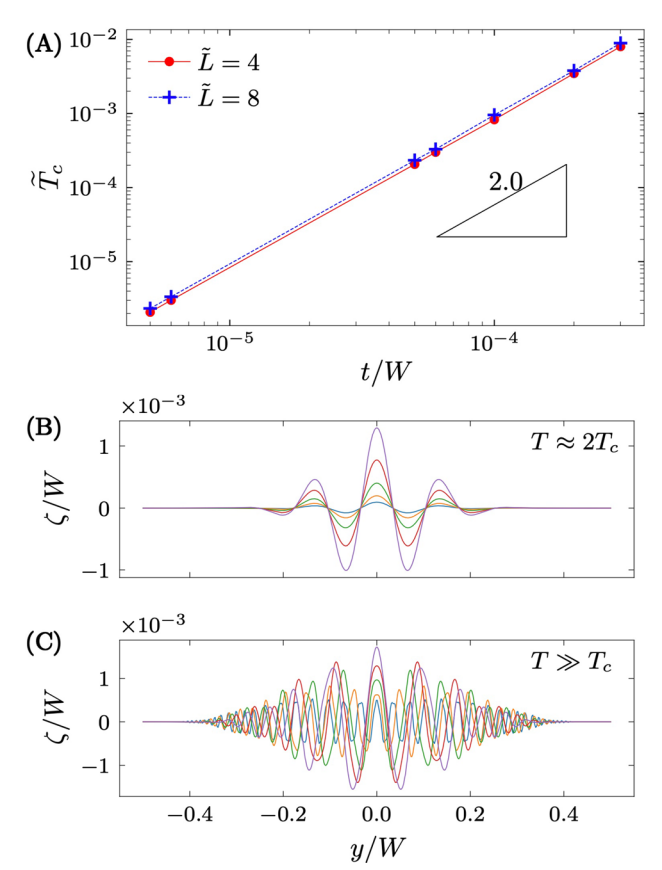


Fig. 7 a The instability threshold \tilde{T}_c , of a long stretched rectangular sheet with clamped edges (model A with L =8W), as obtained from our SE simulations, plotted versus the thickness, $\frac{t}{W}$. The threshold value is shown to be proportional to $(\frac{t}{W})^2$, with a proportionality constant that depends weakly on the aspect ratio $\frac{W}{L}$ for $L \gg W$. This result indicates that the instability is an Euler-like buckling, due to a compressed zone of width $\sim W$, where the compression is, $\sigma_{yy} \sim -T$ (see text). **b** The transverse profile of the shape (at $x \approx x_{max}$, where the compression is maximal), plotted close to threshold. From top to bottom: $t/W = \{32, 16, 8, 4, 2\} \times 10^{-5}$. The plots indicate that the critical wavelength, λ_c , is a finite, thicknessindependent fraction of the sheet width, in accord with Euler buckling instability. c As the exerted tension T is increased beyond T_c , the energetically favorable wavelength λ becomes smaller (in comparison to λ_c), and develops explicit dependence on the sheet thickness. This bucklingto-wrinkling trend is consistent with a transition from nearthreshold to far-from-threshold behavior envisioned in [6]. The profiles are shown for y = 0. From top to bottom: $T/T_c \approx 66$, 118, 266, 1074, 4324

4 Beyond threshold

Upon increasing the control parameter T in model A substantially above its threshold value (13), our simulations (Fig. 7c) show that the near-threshold buckling pattern undergoes two dramatic changes. First, undulations expand (along the \hat{x} -axis) beyond the transversely compressed zone of the planar state. Second, the char-



acteristic wavelength λ becomes substantially smaller than its threshold value $\lambda_c \sim W$. For model B, the analogous process of increasing α beyond threshold (12) does lead to expansion of the deflected zone, but not to any significant reduction in the characteristic undulation wavelength.

A systematic study of this dramatic evolution from a buckling pattern to wrinkles in the (Hookean) far-from-threshold regime ($T_c \ll T \ll Y$) in model A, requires a detailed analysis of the strong effect of wrinkle formation on the stress field in the sheet, and its consequent departure from the planar stress. This non-perturbative effect, which revokes the perturbative approach underlying the near-threshold analysis in Sec. 3, will be the focal point of our subsequent paper. Here, we take a more heuristic approach to rationalize the qualitative distinction between models A and B, by generalizing the analysis in the preceding section beyond the near-threshold regime.

Inspecting the considerations underlying the critical wavelength λ_c (11b), one may notice that the only way in which the planar state is explicitly affecting the wavelength is through the length $\ell \sim W$ of the transversely compressed zone. Assuming that even when the control parameter exceeds considerably the threshold value the wrinkle wavelength λ is affected by the stress distribution through the length ℓ of the actual compressive zone, rule (11b) can be generalized to:

$$\lambda \sim \min\left(W \; , \; \left(\frac{B}{K_{\text{sub}} + T\ell_*^{-2} + B\ell_*^{-4}}\right)^{1/4}\right), \quad (14)$$

where ℓ_* is the *actual* length of the compressive zone (at a given, post-threshold value of the control parameter) rather than its length in the planar state.

With the generalized version (14) of the wavelength rule, one may immediately notice the difference between models A and B. In the former, the presence of longitudinal tension eventually dominates the wavelength, hence:

model A
$$(T \gg T_c)$$
: $\lambda \sim \left(\frac{B}{T\ell_*^{-2}}\right)^{1/4}$ (15)

such that at a fixed value of T/Y, the wavelength λ vanishes with the sheet thickness, signifying a transition from buckling ($\lambda \sim W$ at $T \approx T_c$) to wrinkling ($\lambda \sim t^{1/2} \ll W$ for $T \gg T_c$). The scaling rule of Cerda & Mahadevan [6] is obtained by assuming that the transversely compressed zone extends throughout the whole sheet, i.e., $\ell_* \sim L$ in Eq. (15). In contrast, for model B, the absence of longitudinal tension implies that the pattern does not undergo a similar buckling-to-wrinkling transition as the control parameter α exceeds the threshold value.

The above heuristic argument deserves a healthy dose of skepticism. Why does the transversely compressed zone expand when the sheet is driven away from threshold? Why is it justified to approximate the energetic cost (per area) imposed on undulations by the longitudinal tension as $T(A/\ell_*)^2$? To properly address these questions one has to consider the tension-field solution of this problem, which forms the basis for far-from-threshold analysis, and will be discussed in our subsequent paper.

5 Summary

Focusing on the planar stress of a Hookean, rectangularshaped sheet under uniaxial, longitudinal tensile load, $\sigma_{xx} \approx T$, we showed that the emergence of transversely compressed zones stems from the extension of the pulled clamped edges relative to the bulk. Specifically, we showed that an identical profile of the transverse stress is realized by directly pulling the corners transversely without longitudinal tension (Fig. 1c). This observation evinces that the classic Poisson effect, namely "tensioninduced contraction" of a solid sheet, must not be confused with "tension-induced compression" which underlies tensional wrinkling phenomena. The former is a bulk effect, whereby transverse strain $(\varepsilon_{yy} \sim -\nu T/Y)$ emerges away from the edges in order to avoid compression; The latter is a boundary effect, which can be eliminated by tailoring the boundary conditions (e.g., unclamping the pulled edges), and hence should be referred to as "edge-induced (transverse) compression."

Furthermore, we showed that edge-induced transverse compression stems from a non-monotonic decay of the Airy potential away from the edge, reflecting the effect of complex eigenvalues of the bi-harmonic equation, in analogy to Moffatt eddies in viscous driven cavity flow.

Finally, we showed that localized, transversely compressed zones in the planar stress give rise to buckling instability, with a critical wavelength λ_c proportional to the sheet width W and independent on its thickness t, and a threshold tension $T_c \sim (\frac{t}{W})^2 Y$. Both of these relations mirror the classical Euler buckling, revealing the anticipation of Cerda & Mahadevan [6] that the commonly observed wrinkling pattern in this set-up, with a wavelength λ that vanishes with t (Figs. 1g, 7c), cannot be described by a standard post-buckling theory that assumes moderate perturbation of the planar stress. A description of this wrinkling pattern through a far-from-threshold framework is the subject of a subsequent publication.

Acknowledgements We thank F. Brau, E. Cerda, J. Chopin, P. Damman, A. Kudroli, and N. Menon for valuable discussions. This research was funded by the National Science Foundation under Grant DMR 1822439. Simulations were performed in the computing cluster of Massachusetts Green High Performance Computing Center (MGHPCC).



Author contribution statement

Both authors contributed equally to this paper.

A Solution of planar stress

In this Appendix, we describe the detailed solution of model B with BCs (6e-6h). In our analysis we follow closely the calculation of Benthem [22], who employed Laplace transformation to compute the stress at the clamped edge. Here we go beyond Benthem solution by performing an inverse Laplace transformation, which is required to evaluate the stress in the whole sheet.

A.1 The singularities in the corners

Let us consider first the vicinity of one corner of the sheet in Fig. 1a, where one edge is clamped and the other one is free, and solve Eq. 4 in polar coordinates (r, θ) , see Fig. 8, which depicts the left bottom corner.

$$\left(\frac{\partial^2}{\partial r^2} + \frac{1}{r}\frac{\partial}{\partial r} + \frac{1}{r^2}\frac{\partial^2}{\partial \theta^2}\right)^2 \Phi = 0 \tag{16}$$

BCs Eqs. (5b, 5c) now become

free boundary(
$$\theta = 0$$
): $\sigma_{r\theta} = \sigma_{\theta\theta} = 0$, (17a)

clamped boundary(
$$\theta = \frac{\pi}{2}$$
): $u_r = u_\theta = 0$. (17b)

The general solution of Eq. 16 is

$$\Phi(r,\theta) = r^{\gamma+1} (D_1 \sin(\gamma+1)\theta + D_2 \cos(\gamma+1)\theta + D_3 \sin(\gamma-1)\theta + D_4 \cos(\gamma-1)\theta)$$
(18)

Notice that Eq. (18) has 4 unknowns D_i , such that the four BCs (17) give rise to a nonzero solution only if the determinant of the corresponding 4×4 matrix vanishes, yielding:

$$\sin^2\left(\gamma \frac{\pi}{2}\right) = \frac{4 - \gamma^2 (1 + \nu)^2}{(3 - \nu)(1 + \nu)} \ . \tag{19}$$

For a sheet with positive Poisson's ratio, $\nu > 0$, the solution of Eq. (19) is $\gamma < 1$, such that:

$$\sigma \sim \frac{\partial \Phi}{\partial r^2} \sim r^{\gamma - 1} ,$$
 (20)

and hence the components of stress tensor diverge at the corner (i.e., $r \to 0$). For convenience, we choose to focus

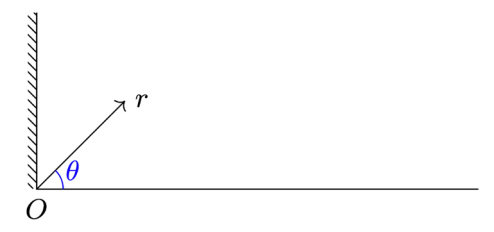
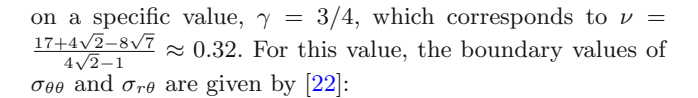


Fig. 8 A corner of a rectangular sheet. We set the corner as the origin of polar coordinates



$$\sigma_{\theta\theta} \left(\theta = \frac{\pi}{2} \right) = c_1 r^{-\frac{1}{4}}, \qquad \sigma_{r\theta} \left(\theta = \frac{\pi}{2} \right) = -c_2 r^{-\frac{1}{4}}$$

$$c_1 = \sqrt{8 + 3\sqrt{7}} c_2 \tag{21}$$

A.2 Laplace transformation

Let us address now the Airy potential in a semi-infinite sheet (Fig. 9). For convenience, we set the width W=2 (i.e., $y\to \frac{y}{2W}, x\to \frac{x}{2W}$), and transform the origin of the coordinate system to the middle of left edge, such that the left clamped boundary is x=0 and the two free boundaries are $y=\pm 1$. To solve Eq. (4), we employ Laplace transformation,

$$f(p,y) = \int_0^\infty \Phi(x,y)e^{-sx}dx , \qquad (22)$$

such that the transformed Eq. (4) becomes

$$s^{4}f + 2s^{2}\frac{\partial^{2}f}{\partial y^{2}} + \frac{\partial^{4}f}{\partial y^{4}} = s^{3}\Phi(0, y) + s^{2}\frac{\partial\Phi}{\partial x}(0, y)$$
$$+s\left(\frac{\partial^{2}\Phi}{\partial x^{2}}(0, y) + 2\frac{\partial^{2}\Phi}{\partial y^{2}}(0, y)\right)$$
$$+\frac{\partial^{2}\Phi}{\partial x^{3}}(0, y) + 2\frac{\partial^{3}\Phi}{\partial x\partial y^{2}}(0, y) \quad (23)$$

With the up-down symmetry $\Phi(x,y) = \Phi(x,-y)$, the singularities at corners, Eq. (21), and BC (6e), we can assume [22]

$$\frac{\partial^2 \Phi}{\partial y^2} = \sigma_{xx}(0, y) = c_1 \{ (1 - y)^{-\frac{1}{4}} + (1 + y)^{-\frac{1}{4}} - 2^{-1/4} \} + \sum_{n=1} a_n \cos(q_n y)$$

$$\frac{\partial^2 \Phi}{\partial x \partial y} = -\sigma_{xy}(0, y) = c_2 \{ (1 - y)^{-\frac{1}{4}} - (1 + y)^{-\frac{1}{4}} + y 2^{-1/4} \} + \sum_{n=1} b_n \sin(k_n y)$$
(24)

where $q_n = (2n-1)\frac{\pi}{2}$, $k_n = n\pi$ and a_n , b_n are constants that must be computed. Equation (24) and the BCs (6g, 6h) enable us to express all boundary terms in the right

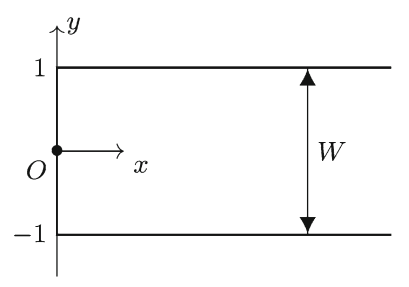


Fig. 9 The configuration of a semi-infinite sheet $(L \to \infty)$. We set the width W=2 for convenience, the left boundary x=0 is clamped and the two boundaries $y=\pm 1$ are free



side of Eq. (23) in terms of the unknowns c_1, c_2 and a_n, b_n , whereas the BCs (6e, 6f) become:

$$f(s, y = \pm 1) = 0 (25a)$$

$$\frac{\partial f}{\partial y}(s, y = \pm 1) = 0 . {(25b)}$$

The solution f(s, y) to Eq. (23) can now be expressed in the following form [22]:

$$f(s,y) = g(s,y)$$

$$-2g(s,1)\frac{(s\cos s + \sin s)\cos sy + s(\sin s)y\sin sy}{\sin 2s + 2s}$$

$$+2\frac{\partial g}{\partial y}(s,1)\frac{(\sin s)\cos sy - (\cos s)y\sin sy}{\sin 2s + 2s}$$
(26)

where g(s,y) is the particular solution of the non-homogeneous ODE (23), while the left two terms correspond to solutions of the homogeneous equation (i.e., replacing the right side with 0), which enable satisfying the BCs (25). The function g(s,y) is relatively complicated, and in order to express it compactly we define an "auxiliary" function:

$$R(q; s, y) = \frac{1}{4s^{4+2q}} \left(e^{isy} (-is)^{q} ((-1+isy)\Gamma(1+q; is) + (1-isy)\Gamma(1+q; isy) - \Gamma(2+q; is) + \Gamma(2+q; isy) \right) + e^{-isy} (is)^{q} ((-1-isy)\Gamma(1+q; -is) + (1+isy)\Gamma(1+q; -isy) - \Gamma(2+q; -is) + \Gamma(2+q; -isy)) \right)$$
(27)

where $\Gamma(x;y)$ is the incomplete gamma function. Then g(s,y) can be written as

$$g(s,y) = \frac{s^3 c_1}{1.3125} \left(R\left(\frac{7}{4}; s, 1 - y\right) + R\left(\frac{7}{4}; s, 1 + y\right) \right)$$

$$-\frac{4}{3} s^2 c_2 \left(R\left(\frac{3}{4}; s, 1 - y\right) + R\left(\frac{3}{4}; s, 1 + y\right) \right)$$

$$+ s(2 + \nu) c_1 \left(R\left(-\frac{1}{4}; s, 1 - y\right) + R\left(-\frac{1}{4}; s, 1 + y\right) \right)$$

$$-\frac{1}{4} \nu c_2 \left(R\left(-\frac{5}{4}; s, 1 - y\right) + R\left(-\frac{5}{4}; s, 1 + y\right) \right)$$

$$+ \left(-s^3 c_1 2^{-\frac{5}{4}} + s^2 c_2 2^{-\frac{5}{4}} \right) \frac{s^2 y^2 - 4}{s^6}$$

$$+ \frac{c_1}{s} \left(2^{-\frac{5}{4}} - \frac{2^{\frac{7}{4}}}{1.3125} \right) - \frac{2 + \nu}{s^3} c_1 2^{-\frac{1}{4}}$$

$$- \frac{\nu}{s^4} c_2 2^{-\frac{1}{4}} + \frac{\alpha}{s^3} + \frac{b_0}{s^2}$$

$$+ \sum_{s=1}^{\infty} \frac{-\frac{s^3}{q_n^2} + s(2 + \nu)}{(s^2 - q_n^2)^2} a_n \cos q_n y - \frac{\frac{s^2}{k_n} + \nu k_n}{(s^2 - k_n^2)^2} b_n \cos k_n y$$

where b_0 is an integration constant:

$$\frac{\partial \Phi}{\partial x}(0,y) = \int \frac{\partial^2 \Phi}{\partial x \partial y}(0,y) dy + b_0.$$
 (29)

A.3 Solution of Laplace transform and its inversion

Next we must solve all unknowns a_n, b_n, c_1, b_0 that define the function g(s, y), Eq. (28), substitute it in Eq. (26)

to obtain the Laplace transform f(s, y), and perform the inverse transform

$$\Phi(x,y) = \frac{1}{2i} \int_{c-i\infty}^{c+i\infty} f(s,y)e^{sx} ds \qquad (c>0) \qquad (30)$$

to obtain the Airy potential $\Phi(x,y)$.

Recalling that our analysis here assumes a semi-infinite sheet, for which we expect the stress potential $\Phi(x,y)$ vanishes exponentially away from the clamped edge at x=0, we note that the Laplace transform f(s,y) must not have any poles at the right half of complex plane $\text{Re}\,(s)>0$. Inspection of Eqs. (26, 28) reveals that the only poles originate from the contribution of the homogeneous solutions of Eq. (23), namely, complex numbers s which solve the nonlinear equation:

$$\sin 2s + 2s = 0. \tag{31}$$

This equation has an infinite sequence of solutions in the right half plane, $\{s_i \text{ and } \bar{s}_i; i \in \mathbb{N}, \operatorname{Re}(s_i) > 0, \operatorname{Im}(s_i) > 0\}$, which can be arranged in increasing order, $|s_{i+1}| > |s_i|$. Requiring the residues of f(s,y) at s_i and \bar{s}_i to vanish, yields an infinite sequences of algebraic equations

Res
$$f(s_i, y) = 2\left(\frac{\partial g}{\partial y}(s_i, 1) - g(s_i, 1)\sin^2 s_i\right)G(s_i, y) = 0,$$
(32)

where we used Eqs. (26, 28) and defined

$$G(s_i, y) = \frac{(\sin s_i)\cos s_i y - (\cos s_i)y\sin s_i y}{4\cos^2 s_i} . \tag{33}$$

Equations (32, 28), together with the complementary set of conjugate equations for the residues $\operatorname{Res} f(\bar{s}_i, y) = \overline{\operatorname{Res} f(s_i, y)}$, determine the unknowns a_n, b_n, c_1, b_0 in Eq. (28), and thereby the Laplace transform f(s, y) through Eq. (26). In order to obtain a numerical solution of this system of equations, we truncate the sequence of unknowns, and keep only the 1000 leading unknowns (ordered by increasing magnitude of the corresponding poles $|s_i|$).

Furthermore, in order to carry out the integration in Eq. (30), we can close the contour in the left half complex plane Re (s) < 0 and compute it through the sum of residues of f(s,y). Noticing that the poles of f(s,y) in the complex s plane are solutions of Eq. (31), one readily realizes that the poles in the left half of the complex plane are $\{-s_i, -\bar{s}_i\}$, and consequently:

$$\Phi(x,y) = \sum_{i=1} \operatorname{Res} \left(\left(f(s,y)e^{sx}; -s_i \right) + \operatorname{Res} \left(f(s,y)e^{sx}; -\bar{s}_i \right) \right)$$

$$= 4\operatorname{Re} \sum_{i=1} \left(g(-s_i, 1)\sin^2 s_i - \frac{\partial g}{\partial y}(-s_i, 1) \right) G(s_i, y)e^{-s_i x}$$
(34)

Finally, recovering our transformation $y \to \frac{2y}{W}$, $x \to \frac{2x}{W}$ and define $p_i = 2s_i$, we can get Eq. (9b)

$$\Phi(x,y) = \operatorname{Re}\left\{\sum_{i} C_{i} \cdot \left(\Phi^{i,c}(x,y) + A_{i}\Phi^{i,s}(x,y)\right)\right\},$$

$$C_{i} = \frac{\sin\frac{p_{i}}{2}}{\cos^{2}\frac{p_{i}}{2}} \left(g(-\frac{p_{i}}{2},1)\sin^{2}p_{i} - \frac{\partial g}{\partial y}(-\frac{p_{i}}{2},1)\right) \quad (35)$$

References

- N. Friedl, F. Rammerstorfer, F. Fischer, Computers and Structures 78, 185 (2000)
- E. Cerda, K. Ravi-Chandar, L. Mahadevan, Nature 419, 579 (2002)
- 3. V. Nayyar, K. Ravi-Chandar, R. Huang, International Journal of Solids and Structures 48, 3471 (2011)
- S.T. Milner, J.F. Joanny, P. Pincus, Euro. Phys. Lett. 9, 495 (1989)
- N. Bowden, S. Brittain, A.G. Evans, J.W. Hutchinson, G.M. Whiteside, Nature 393, 146 (1998)
- E. Cerda, L. Mahadevan, Phys. Rev. Lett. 90, 074302 (2003)
- 7. H. Wagner, Z Flugtechn Motorluftschiffahrt 20, 8 (1929)
- 8. M. Stein, J.M. Hedgepeth, Technical report, NASA (1961)
- 9. E.H. Mansfield, *The Bending and Stretching of Plates* (Cambridge University Press, 1989)
- 10. A.C. Pipkin, IMA J. Appl. Math. 36, 85 (1986)
- D.J. Steigmann, Proc. Roy. Soc. London A. 429, 141 (1990)
- J.D. Paulsen, Annual Review of Condensed Matter Physics 10, 431 (2019)
- 13. D. Vella, Nat. Rev. Physics 1, 425 (2019)

- 14. K.A. Brakke, Exp. Math. 1, 141 (1992)
- T.J. Healey, Q. Li, R.B. Cheng, J. Nonlin. Sci. 23, 777 (2013)
- Q. Li, T.J. Healey, J. Mech. Phys. Solids 97, 260 (2016), symposium on Length Scale in Solid Mechanics - Mathematical and Physical Aspects, Inst Henri Poincare, Paris, FRANCE, JUN 19–20, 2014
- A.A. Sipos, E. Feher, Int. J. Solids. Struct. 97–98, 275 (2016)
- C. Fu, T. Wang, F. Xu, Y. Huo, M. Potier-Ferry, J. Mech. Phys. Solids 124, 446 (2019)
- T. Wang, C. Fu, F. Xu, Y. Huo, M. Potier-Ferry, Int. J. Eng. Sci. 136, 1 (2019)
- A. Panaitescu, M. Xin, B. Davidovitch, J. Chopin, A. Kudrolli, Phys. Rev. E 100, 053003 (2019)
- L.D. Landau, E. Lifshitz, Theory of Elasticity (Pergamon, New York, 1986)
- J.P. Benthem, The Quarterly Journal of Mechanics and Applied Mathematics 16, 413 (1963)
- 23. D.A. Spence, IMA. J. App. Math. 30, 107 (1983)
- J. Chopin, A. Panaitescu, A. Kudrolli, Phys. Rev. E 98, 043003 (2018)
- 25. H.K. Moffatt, J. Fluid. Mech. 18, 1 (1964)
- P.N. Shankar, M.D. Deshpande, Annual Review of Fluid Mechanics 32, 93 (2000)

